nature catalysis

Article

https://doi.org/10.1038/s41929-024-01147-y

Dinuclear Cu(I) molecular electrocatalyst for CO_2-to-C_3 product conversion

Received: 7 September 2022

Accepted: 14 March 2024

Published online: 15 April 2024

Check for updates

Naonari Sakamoto ✉, Keita Sekizawa ✉, Soichi Shirai, Takamasa Nonaka, Takeo Arai, Shunsuke Sato & Takeshi Morikawa

Molecular metal complex catalysts are highly tunable in terms of their CO_2 reduction performance by means of their flexible molecular design. However, metal complex catalysts have challenges in their structural stability and it has not been possible to synthesize high-value-added C_3 products due to their inability to perform C–C coupling. Here we show a CO_2 reduction reaction catalysed by a Br-bridged dinuclear Cu(I) complex that produces C_3H_7OH with high robustness during the reaction. The C–C coupling reaction mechanism was analysed by experimental operando surface-enhanced Raman scattering analysis, and theoretical quantum-chemical calculations proposed the formation of a C–C coupling intermediate species with substrate incorporation between the two Cu centres. Molecular design guidelines based on this discovery offer an approach to developing next-generation catalysts that generate multicarbon CO_2 reduction products.

The electrochemical carbon dioxide reduction reaction (CO_2RR), which is used to produce valuable chemical feedstocks and fuels, is a promising technology for storing renewable energy in response to the increasing urgency to develop and implement a sustainable carbon-neutral economy[1]. CO_2RR technology can substantially reduce the use of fossil-fuel raw materials and contribute to controlling the anthropogenic carbon cycle[2–5]. Ideally, CO_2 should be adsorbed and retained in the vicinity of the catalyst, then the catalytic reaction should proceed, and the reaction intermediates should be retained until the required reduction products are formed[6,7]. It is also necessary to efficiently transfer multiple electrons and protons to the CO_2 (ref. 8). In general, reductants that require more electrons are preferred product targets because of their higher energy densities and larger markets[2–4]. Multicarbon (C_{2+}) products such as ethylene and ethanol, which require C–C coupling reactions, are noteworthy among these[2], but products with even higher energy density that require additional C–C coupling, such as C_3H_7OH, are even more valuable[2,7]. It is thus desirable for a CO_2 conversion catalyst with high efficiency to have various functions and to be strictly controllable and adjustable via, for example, structural features related to the C–C coupling reaction[9].

Molecular catalysts can provide various added functions as a result of differences in their molecular structure, and they have the potential to solve the major challenge of the selective reduction of CO_2 to a specific product[10–13]. Unimolecular metal complex catalysts can freely modulate reactivity and selectivity by changing the design of the ligand, unlike single-metal-atom nitrogen-doped carbon[14] and coordination polymers[15–17]. Indeed, a molecular-catalysed CO_2RR process has already been achieved to provide the selective generation of different C_1 products (such as CO and HCOOH) by changing the central metal's electronic state through the selection of appropriate organic ligands[18–20]. The difference in electronic states enables control of the adsorption structure of the reaction intermediates as well as the efficiency of proton addition[13–20]. Nevertheless, only a few cases of C_2 product formation on molecular catalysts[21–25], and no cases of C_3 product formation, have been reported. The molecular catalysts used thus far have been almost exclusively mononuclear. Because CO_2 itself exhibits very low reactivity, CO_2 can only act on the active metal centre[18–20], and it is unlikely that another CO_2 will react directly with the CO_2-reduced species on the metal centre of a mononuclear complex to induce coupling. The synthesis of C_{2+} products is assumed to require the reduction of at least two CO_2 molecules nearby, followed by coupling between the reductive species. For this reason, multinuclear molecular catalysts are promising CO_2RR catalysts for C_{2+} formation[21,22].

Toyota Central R&D Labs Inc, Nagakute, Aichi, Japan. ✉e-mail: naonari@mosk.tytlabs.co.jp; sekizawa@mosk.tytlabs.co.jp

Promoting a CO_2 feed in the vicinity of the catalyst is also important in the formation of C_2 products, which require C–C coupling reactions[7,26]. Recent studies have suggested that the efficiency of the CO_2 supply can be increased by using a gas diffusion cell[4,6,7]. The catalyst itself must be capable of adsorbing and then retaining CO_2 in the vicinity of the catalyst to maintain the feed. CO_2 retention is accomplished with materials that exhibit hysteresis properties in the adsorption–desorption process based on physical and chemical interactions between the CO_2 and the adsorbent material[27]. Reversible CO_2 adsorption is surface-area-dependent[27] and has been demonstrated for many materials[22,24]. In the case of molecular catalysts, the reversible adsorption capacity, which is pressure-dependent, is insufficient to retain CO_2 in the vicinity of the catalyst. A molecular design is thus needed to form a complex of CO_2 that can retain CO_2 with an interaction stronger than the physical adsorption interaction, without applying electrical energy. The improved efficiency of the primary process (that is, contact between CO_2 and the catalyst) of such molecules is expected to lead to a lower activation energy and improved selectivity. The ability of molecular catalysts to adsorb and retain CO_2 can be enhanced by introducing amine groups[28,29] or π-conjugated substituents to the catalyst ligand[30,31]. It has been suggested that this CO_2 retention ability alone is not sufficient for the formation of C_3 products, and the reaction intermediates must also demonstrate retention ability[7]. Unfortunately, the molecular catalysts that have been reported to induce C_2 formation have also been observed to decompose too rapidly under operating conditions[23–25]. Accordingly, robustness is also necessary to maintain the superior features of precisely designed molecular catalysts.

In this Article, to develop a catalyst capable of C_3 product formation, we report the design a molecular catalyst with a ligand that has a large number of π electrons and robust active sites. Specifically, we use Cu multinuclear metal complexes with a Br bridging ligand. Adsorption–desorption hysteresis due to CO_2 adsorption and retention was observed in the metal complexes with close Cu active centres. Operando X-ray absorption fine structure (XAFS) analysis confirmed that the precisely designed structure does not decompose during CO_2 electrolysis in an aqueous solution, and C_3 production from CO_2 was achieved using this engineered molecular catalyst. In addition, important intermediates resulting from C–C coupling were observed via operando spectroscopic analysis, and density functional theory (DFT) calculations strongly supported the derived mechanism, suggesting the validity of the concept of C_3 production by the multinuclear molecular catalyst.

Results

Synthesis of CuBr molecular catalysts and characterization

We synthesized di- or trinuclear Cu(I) molecular metal complexes. Specifically, we synthesized $[Cu_3(\mu\text{-}Br)_2(\text{bis-methyl-bisphenylphosphine})_3]Br^-$ (CuBr–BisM)[32–34], $Cu_2(\mu\text{-}Br)_2(\text{1,2-phenyl-bisphenylphosphine})_2$ (CuBr–12B)[35,36] and $Cu_2(\mu\text{-}Br)_2(\text{triphenylphosphine})_2(\text{4-phenylpyridine})_2$ (CuBr–4PP)[37] (Fig. 1a). The structures of the obtained Cu(I) complexes were analysed by single-crystal X-ray diffraction analysis (Fig. 1a and Supplementary Fig. 1). CuBr–12B and CuBr–4PP were confirmed to be the desired Br-bridged dinuclear complex by matching the unit cells in the single-crystal analysis with previous reports[35–37]. CuBr–BisM (Supplementary Tables 2–9) is consistent with the previously reported trinuclear structure, except for the solvent molecules in the crystal[32–34].

Figure 1b,c shows the CO_2 adsorption–desorption behaviour of powdered samples of the molecular metal complexes. CuBr–BisM and CuBr–12B (Fig. 1b) adsorbed more CO_2 than the raw material, CuBr (Fig. 1c), but almost no hysteresis was observed. The results show that these complexes do not retain CO_2. By contrast, CuBr–4PP exhibited hysteresis in the adsorption–desorption process (Fig. 1c). CO_2 is known to interact with the π orbitals of phenyl and pyridine moieties[30,31]. The CuBr–4PP is assumed to have gained the ability to adsorb and retain CO_2 as a result of the strong interaction of the phenyl group with CO_2, which is not involved in the coordination.

Cyclic voltammetry experiments were conducted on monomeric molecules to investigate the electrochemical properties of the synthesized molecular catalysts in homogeneous systems. In experiments under an Ar atmosphere, the first reduction wave was observed at −1.2 V versus $Ag/AgNO_3$ for all the metal complexes (Fig. 1d–f and Supplementary Fig. 2). The first reduction wave was found to be a one-electron reduced species under an Ar atmosphere (Supplementary Fig. 3). The lowest unoccupied molecular orbitals (LUMOs) of CuBr–BisM and CuBr–12B are mainly distributed on the P atoms and the phenyl groups and are partially distributed over the central Cu_2Br_2 moiety. By contrast, the LUMO of CuBr–4PP is localized on the 4-phenylpyridine (4PP) ligand moieties (Supplementary Fig. 4). In situ UV–vis spectra also confirmed that it was a ligand reduction (Supplementary Fig. 5). The first reduction wave is attributed to electron injection into the LUMO moiety. CuBr–BisM exhibited similar current profiles under CO_2 and Ar atmospheres, with no current increase indicative of a catalytic current due to CO_2 reduction (Fig. 1d). The voltammogram for CuBr–12B shows a catalytic wave starting from the same potential as that for electron injection into the 12B ligands, with behaviour similar to that of a typical CO_2-reducing molecular catalyst (Fig. 1e). However, in the voltammogram for CuBr–4PP, the reduction wave was observed in the region from −1.0 to −1.1 V, which is lower than the potential at which electrons enter the phenyl and pyridine sites of the 4PP ligand (Fig. 1f). A more negative sweep did not increase the current, and the catalytic current for CO_2 reduction was observed at potentials more negative than −1.8 V versus $Ag/AgNO_3$. The results also suggest that a molecule designed to retain CO_2 would also affect the reduction potential. Operando X-ray absorption near-edge structure (XANES) analysis in MeCN solution confirmed that the Cu(I) state is maintained (Supplementary Fig. 6). Apparently, the association complex CuBr–4PP retains the CO_2-reduced species as the active species without releasing them after accepting electrons, and functions as a catalyst to generate reduced products through further reduction of the active species when a potential more negative than −1.8 V is applied.

Investigation of CO_2 electroreduction for CuBr molecular catalysts

We investigated the activity of the CuBr molecular catalyst electrodes by performing heterogeneous electrochemical CO_2RRs in a 0.5 M $KHCO_3$ electrolyte (Supplementary Figs. 7 and 8) using an H-type cell. Powdered crystals of each CuBr molecular metal complex were applied to one side of carbon paper (CP) to fabricate electrodes. Figure 2a shows the Faradaic efficiencies for all the products obtained during the CO_2RR using the CuBr–4PP electrode. At −1.4 V versus Ag/AgCl, the Faradaic efficiency of H_2 production was ~60% and that of HCOOH, which was the main product of CO_2 reduction, was ~20%. The efficiency of CO production was only 4%, whereas that of C_2H_5OH production was ~10%. C_2H_5OH was the product formed at the lowest potential among the CO_2 reduction products requiring C–C coupling. At −1.6 V versus Ag/AgCl, the formation of C_3H_7OH, C_2H_4 and CH_4 was confirmed. At −2.2 V versus Ag/AgCl, the production efficiency of the C_{2+} products in total was 60% and that of C_3H_7OH was ~10%. The formation of C_3H_7OH has therefore been successfully demonstrated on a molecular catalyst (Supplementary Table 1). The efficiency of CO formation[6,8], which is considered an intermediate of C_{2+} products, was less than 10% at all potentials within the investigated range. The current flowed stably for 6 h (Supplementary Fig. 9), and the reduction products were also produced stably. The carbon source for the C_{2+} products generated over CuBr–4PP was identified as the introduced gaseous CO_2 by isotope tracer experiments using $^{13}CO_2$ (Supplementary Fig. 10).

Supplementary Fig. 11 presents the Faradaic efficiencies at each potential for CuBr–BisM and CuBr–12B. Figure 2b–d compares the Faradaic efficiencies at −2.2 V versus Ag/AgCl for CuBr–4PP, CuBr–BisM

https://doi.org/10.1038/s41929-024-01147-y

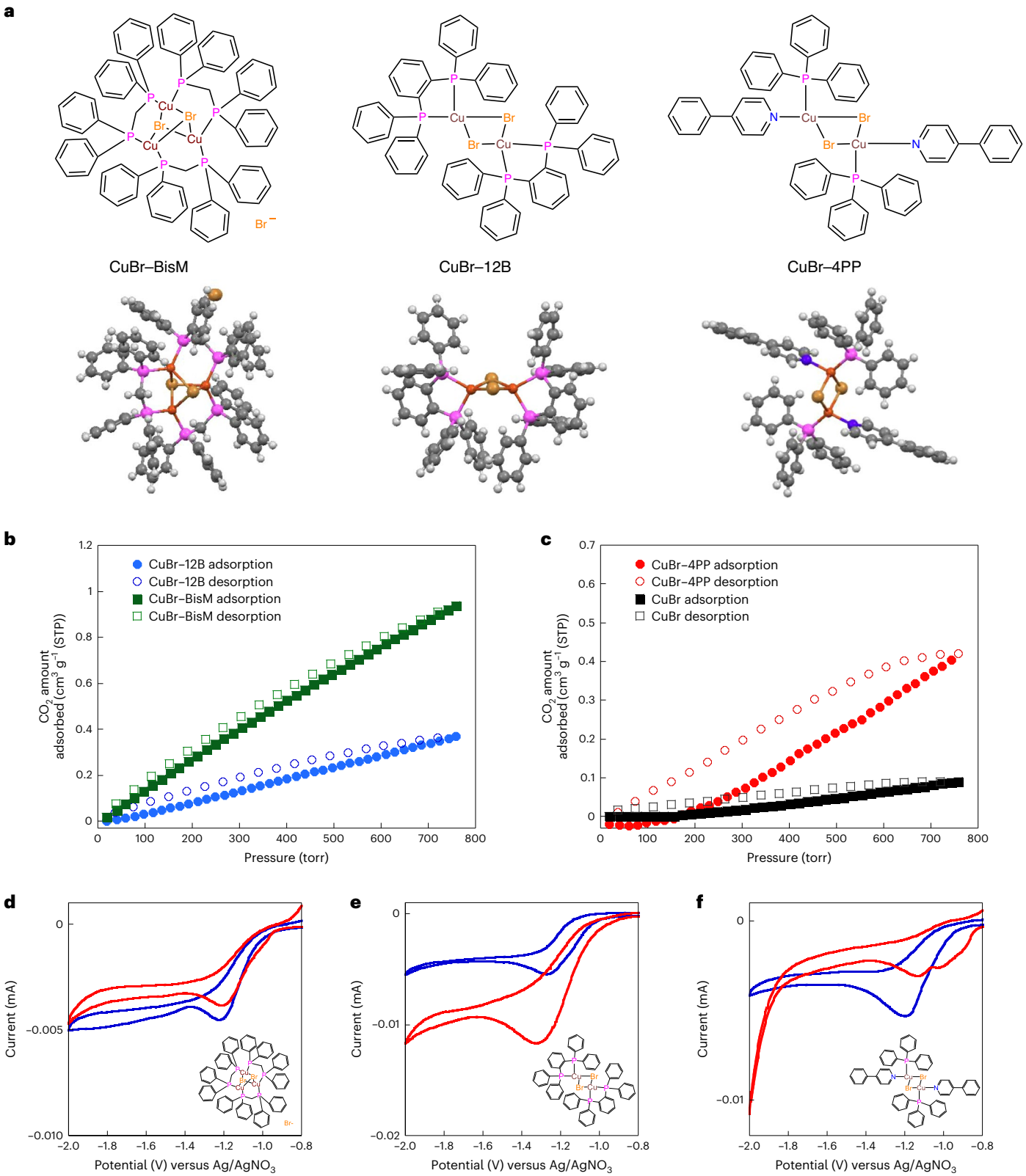

Fig. 1 | Cu(I) molecular structure and characterization. a, Molecular structures of $[Cu_3(\mu\text{-}Br)_2(\text{bis-methyl-bisphenylphosphine})_3]Br^-$ (CuBr–BisM), $Cu_2(\mu\text{-}Br)_2(1,2\text{-phenyl-bisphenylphosphine})_2$ (CuBr–12B) and $Cu_2(\mu\text{-}Br)_2(\text{triphenylphosphine})_2(4\text{-phenylpyridine})_2$ (CuBr–4PP). Solvent molecules are not shown in the figure. The crystal parameters and refinement data for the CuBr metal complexes are shown in Methods, Supplementary Fig. 1 and Supplementary Tables 2–9. **b**, CO_2 adsorption and desorption spectra of CuBr–12B and CuBr–BisM at room temperature. **c**, CO_2 adsorption and desorption spectra of CuBr–4PP and copper(I) bromide at room temperature. **d**–**f**, Cyclic voltammograms for 0.5 mM CuBr–BisM (**d**), 0.5 mM CuBr–12B (**e**) and 0.5 mM CuBr–4PP (**f**), measured in acetonitrile (MeCN) solution containing 0.1 M $NEt_4^+BF_4^-$ under Ar (blue) or CO_2 (red). The measurements were conducted in a voltage range from −0.8 to −2.0 V using a glassy carbon working electrode, a Pt counter electrode and a $Ag/AgNO_3$ reference electrode. Scan rate, 25 mV s^{-1}.

https://doi.org/10.1038/s41929-024-01147-y

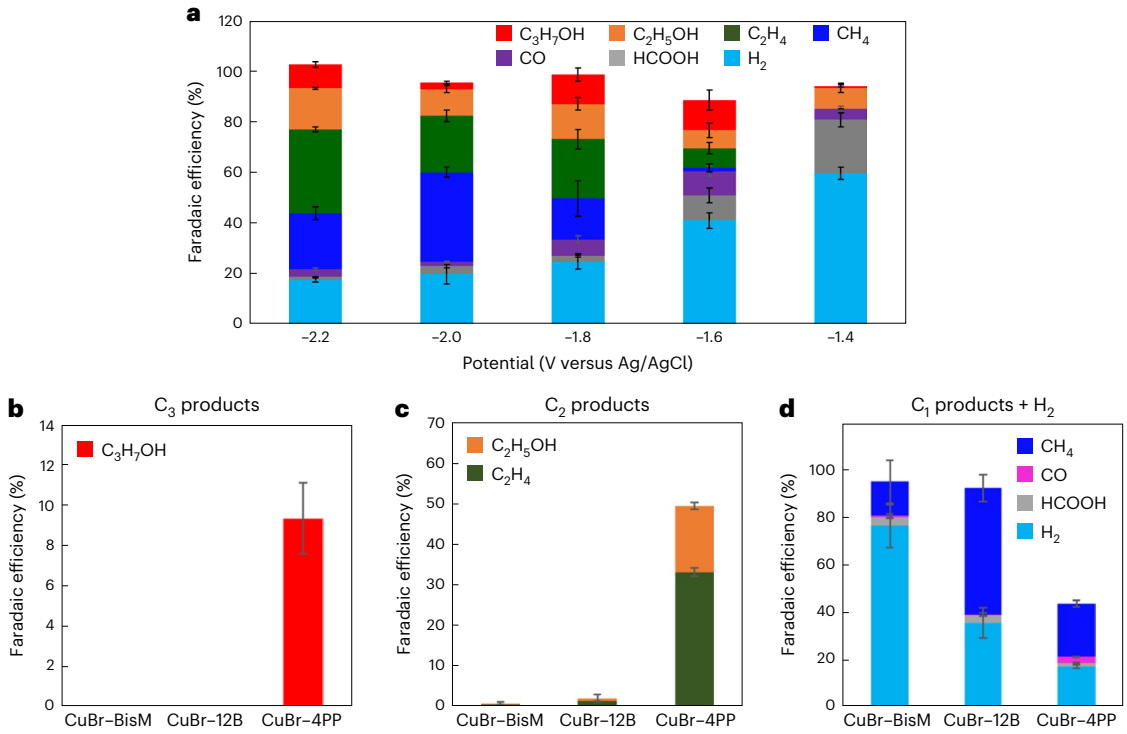

Fig. 2 | Electrochemical CO_2 reduction for Cu(I) molecular catalyst. a, Faradaic efficiency of different reduction products was observed after 1 h of CO_2 reduction using the CuBr–4PP electrodes in a 0.5 M $KHCO_3$ electrolyte. **b**–**d**, Faradaic efficiencies of various reduction products (C_3 (**b**), C_2 (**c**), $C_1 + H_2$ (**d**)) observed at −2.2 V versus Ag/AgCl after CO_2 reduction for 1 h using the CuBr–BisM, CuBr–12B and CuBr–4PP electrodes in the same electrolyte. Error bars correspond to the standard error of three independent measurements.

and CuBr–12B. For CuBr–BisM, which exhibits no CO_2 adsorption capacity and for which cyclic voltammograms recorded in organic solvents show no CO_2 reduction wave, the Faradaic efficiency for the production of H_2, which is the main product, was ~80%, and that for the production of CH_4 was ~20%. These results indicate that the C–C coupling reaction was not proceeding. For CuBr–12B, which did not exhibit CO_2 adsorption but whose cyclic voltammogram did show a CO_2 reduction wave, the efficiency of H_2 production was suppressed to 40% and that of CH_4 production was ~50%; however, the efficiency of the C_2 products was only several percent. At the same potential, CuBr–4PP was found to produce C_2 products as the main product and to produce C_3H_7OH with 10% Faradaic efficiency, suggesting that the CO_2 adsorption and retention ability and the stable CO_2 association structure complex can contribute to the characteristic CO_2 reduction properties.

To obtain deeper insight into the complex potential dependence of CuBr–4PP, the carbon monoxide reduction reaction (CORR) was performed using CO as substrate, which is more reactive and will contribute as a reaction intermediate[5–9]. The formation of C_3H_7OH by the CORR was confirmed at all potentials from −1.4 V to −2.2 V (Supplementary Fig. 12). The yields of C_3 and C_2 products increased monotonically with potential, and no CH_4 formation was observed at any potential. This suggests that C–C coupling will be induced by CO production in the CO_2RR, but the strong potential dependence of the proton-coupled electron injection process will be accompanied by methane by-products, leading to complex changes in the product ratios.

Investigation of oxidation state and structure during the CO_2RR

Changes in the oxidation state of Cu can be observed by operando XAFS measurements[23], even for Cu molecular catalysts that do not show any changes in ex situ experiments (for example, X-ray photoelectron spectroscopy (XPS), X-ray diffraction and XAFS)[24,25]. Accordingly, we also conducted operando XAFS experiments to investigate the change in the oxidation state of Cu in CuBr molecular catalysts during the CO_2RR (Supplementary Fig. 13a). Supplementary Fig. 13 shows the operando XANES results obtained via fluorescence XAFS experiments for the CuBr molecular catalysts. The Cu in the CuBr–4PP complex (Supplementary Fig. 13b,c) retains the Cu(I) oxidation state during the CO_2RR. In addition, with an applied potential from −1.2 V to −2.4 V versus Ag/AgCl, the oxidation state of Cu in CuBr–4PP did not change (Supplementary Fig. 13h). By contrast, CuBr–BisM and CuBr–12B were shifted to the low-energy side and became close to Cu(0) (Supplementary Fig. 13d–g). The validity of the present analysis was also examined using known metal complex catalysts. HKUST-1 (Cu_3(benzene-1,3,5-tricarboxylate)$_2$) metal–organic frameworks[38] (Supplementary Fig. 13i), which have been reported to change from Cu(II) to Cu(0) within 1 h (ref. 23), were observed to change to Cu(0) within 10 min during the current operando XANES measurements. The measurements are thus considered to have been performed at least as well as those previously reported. From XPS spectra, it was also confirmed that only CuBr–4PP maintained its state before and after the reaction (Supplementary Fig. 14). Calculations based on the structures of CuBr–4PP and CuBr–12B with multiple electrons also indicate that CuBr–12B is less stable than CuBr–4PP, supporting the operando XAFS and ex situ XPS results (Supplementary Table 10). We also used bright-field transmission electron microscopy to observe CuBr–4PP after the CO_2RR and did not observe dark spots indicating the formation of Cu clusters (Supplementary Fig. 15). Dynamic light scattering (Supplementary Fig. 16) and operando Raman (Supplementary Fig. 17) measurements confirmed that no Cu metal was formed from CuBr–4PP. Therefore, both operando and ex situ (Supplementary Fig. 18) spectroscopic analyses and morphological observations show that the oxidation state and structure of CuBr–4PP were maintained during the CO_2RR.

Reaction mechanism by operando analysis and DFT calculations

The structural changes in the ligand moiety during the CuBr–4PP reaction were investigated using operando Raman measurements. The peak intensity at 1,580 cm^{-1}, where the C=C stretching vibrations of the 4PP ligand are observed (Supplementary Fig. 19), was enhanced while applying potential. The enhanced peak intensity indicates that electrons were incorporated into the 4PP ligand moiety when a potential was applied[39] (Supplementary Fig. 20). No other peaks were observed.

Weak peaks, such as those for the reaction intermediates of C_3H_7OH, can be observed by surface-enhanced Raman scattering (SERS) measurements based on the localized surface plasmon resonance of metal nanoparticles (Fig. 3a)[40–42]. Anisotropic Ag plates as localized surface plasmon resonance substrates and an appropriate excitation wavelength were used to obtain stronger SERS signals[40,41]. SiO_2 was used to inactivate Ag to prevent its CO_2RR activity. Figure 3b,c and Supplementary Fig. 21 show the results obtained by operando SERS using Ag-plate core/SiO_2 shell nanoparticles (NPs). In the SERS spectra of CuBr–4PP under a CO_2 atmosphere, peaks were observed at 1,740 and 2,050 cm^{-1} at −1.2 V versus Ag/AgCl (Fig. 3b), a potential at which no reduction products were observed (Supplementary Fig. 22). When the potential was increased to −2.0 V versus Ag/AgCl, peaks were observed near 1,540–1,560 cm^{-1} (Fig. 3c). However, these peaks were not observed when the sample was under an Ar atmosphere (Supplementary Fig. 21a,b). These peaks were not observed in CuBr–12B (Supplementary Fig. 21c,d). Furthermore, labelling experiments with $^{13}CO_2$ confirmed that the operando SERS peak in the CuBr–4PP was derived from CO_2 (Supplementary Fig. 23).

To identify the observed reaction intermediates and to elucidate the reaction mechanism for the formation of C_3 products, DFT calculations were performed with CO as the substrate. This mechanism also gives information regarding the main reaction mechanism in the CO_2RR, because CO was produced as a by-product along with propanol in the CO_2RR (Fig. 2a), and propanol was produced in both the CO_2RR and CORR (Supplementary Fig. 12). For the process from the initial structure of CuBr–4PP ($[Cu–Br–Cu]^0$) to the formation of C_3 intermediate species via the C–C coupling reaction by the CORR, the possible intermediates were searched and selected based on the validity of the free-energy change and the correspondence with the SERS spectrum (Fig. 3f and Supplementary Table 11). The process of transfer of both electrons (ET) and protons (PT) can involve multi-step (PT + ET or ET + PT) or concerted (proton-coupled electron transfer; PCET) mechanisms[43]. Here, we assume that all such processes proceed by a concerted mechanism, and the energy difference required for the process is expressed in terms of potential (E_{PCET}). In the CORR, insertion of CO into the Cu–Br–Cu bridge of the initial structure of CuBr–4PP ($[Cu–Br–Cu]^0$) yielded $[Cu–Br\_CO–Cu]^0$ with a free-energy change (ΔG) of 4.9 kcal mol^{-1}. Transition-state analysis yielded $[Cu–Br\_CO–Cu]^{0‡}$ with an energy difference from $[Cu–Br–Cu]^0$, the activation barrier ($\Delta G^‡$), of 14.0 kcal mol^{-1}. The subsequent Br desorption process (6.2 kcal mol^{-1}) can also proceed immediately at room temperature. Adding one electron and one proton to $[Cu–CO–Cu]^+$ gave $[Cu–CHO–Cu]^+$. This energy difference corresponds to −1.14 V versus the normal hydrogen electrode (NHE), which can proceed under the present experimental conditions. CO insertion into the CHO bridge of $[Cu–CHO–Cu]^+$ gave the structure $[Cu–CHOCO–Cu]^+$. In this transition state, the bridging CHO shifted to one Cu, the inserted CO coordinated to the other Cu, and the activation barrier was 13.0 kcal mol^{-1}. The energy difference between $[Cu–CHOCO–Cu]^+$ and $[Cu–CHOCO–Cu]^0$ was equivalent to +0.27 V versus NHE, which is more positive than the previous electrochemical process, so $[Cu–CHOCO–Cu]^0$ would be produced. In $[Cu–CHOCO–Cu]^0$, the CHO group migrated away from the Cu centre and only the other C was bridged between the Cu atoms. Adding one electron and one proton to $[Cu–CHOCO–Cu]^0$ gave $[Cu–CHOCOH–Cu]^0$ with an energy difference of 0.01 V versus NHE. The insertion of CO into the (CHO)C(OH) bridge produced $[Cu–CHOCOHCO–Cu]^0$, and the activation barrier for this process was 18.7 kcal mol^{-1}. Therefore, all of these electrochemical processes can proceed sufficiently at room temperature, because they can proceed with an activation barrier of less than 20 kcal mol^{-1} if a potential of about −1.2 V versus Ag/AgCl (−1.4 V versus NHE) is applied.

The calculated wavenumbers of those intermediates of the substrate-derived carbon (ν^{12}_{CO} and ν^{13}_{CO} in Supplementary Table 11) had good correspondence with the experimental SERS spectrum in Fig. 3b,c with a small deviation of less than 20 cm^{-1}, except for $[Cu–Br\_CO–Cu]^0$ (ν^{12}_{CO} = 2,126, ν^{13}_{CO} = 2,078 cm^{-1}) and $[Cu–CHOCO–Cu]^+$ (ν^{12}_{CO} = 1,781, ν^{13}_{CO} = 1,741 cm^{-1}). $[Cu–Br\_CO–Cu]^0$ and $[Cu–CHOCO–Cu]^+$ would have changed immediately, because the former has a small energy barrier (6.2 kcal mol^{-1}) to Br desorption and the latter should be reduced at a potential more positive (0.25 V versus NHE) than the applied potential. Because thermal processes with energy barriers above 13 kcal mol^{-1} are relatively slow, the reactant intermediates ($[Cu–CHO–Cu]^+$ and $[Cu–CHOCOH–Cu]^0$) would be observed in operando SERS. Even though the assumed PCET process has a positive energy difference in terms of potential, the actual rate may be slower because it involves not only electrons but also thermal proton supply processes, so reactant intermediates ($[Cu–CO–Cu]^+$ and $[Cu–CHOCO–Cu]^0$) may have been observed. Therefore, to correspond to both the experimental and computational results, we have derived a reaction mechanism for the C–C coupling process of CuBr–4PP to synthesize C_3 species (Fig. 3d). The subsequent supply of electrons and protons would produce the propanol.

In the proposed mechanism, the total charge of the CuBr–4PP molecule changes between 0 and +1 during the CO_2/CORR reactions. The Mulliken charge densities of the Cu centre (obtained by DFT calculations) for each intermediate in this reaction mechanism (Supplementary Table 11) suggest that the Cu state does not change significantly from its initial +1 state to the 0 or +2 state, which is consistent with the operando XAFS results showing that Cu remains in the +1 state. The Cu valence of the active centre effectively remains Cu(I) because the accepted electrons are dispersed into the phenylpyridine and CO_2-reduction intermediate species. This molecular structure that disperses electrons within the ligand may contribute to the suppression of Cu(0) cluster formation.

The excellent agreement between the peaks extracted from the SERS spectra and DFT simulation spectra strongly supports that the computationally inferred reaction mechanism could proceed at room temperature and with applied potential. The transition-state structures resulting from this mechanistic analysis suggest that the key to the progression of C–C coupling in the Cu dinuclear molecular metal complex is forming a CO_2/CO-reduced intermediate species that forms a bridging intermediate between the two Cu active sites. The bridging intermediate can flexibly change the Cu–Cu distance as the reaction proceeds, attracting reducing species to one Cu side and accepting the substrate to the other Cu side. The formation of C_3H_7OH would result from C–C coupling at the bridging site in flexible Cu binuclear structures. Using molecular catalysts allows us to approach the unclear reaction mechanism of C_3 and C_2 product formation[44–49] from both experimental and computational perspectives and may provide another product methodology in the future.

Conclusions

We have synthesized Cu multinuclear complexes directed for C–C coupling. Among these, the dinuclear complex CuBr–4PP enabled the synthesis of not only C_2 products but also C_3 products, by means of CO_2/CORR reactions. The Faradaic efficiency of CuBr–4PP was found to be ~50% for C_2 products and 12% for propanol. Using operando XAFS analysis, we confirmed that, during the CO_2RR, the metal complex structure is maintained without forming Cu metal. The favourable CO_2 adsorption performance brought about by this structure contributes

https://doi.org/10.1038/s41929-024-01147-y

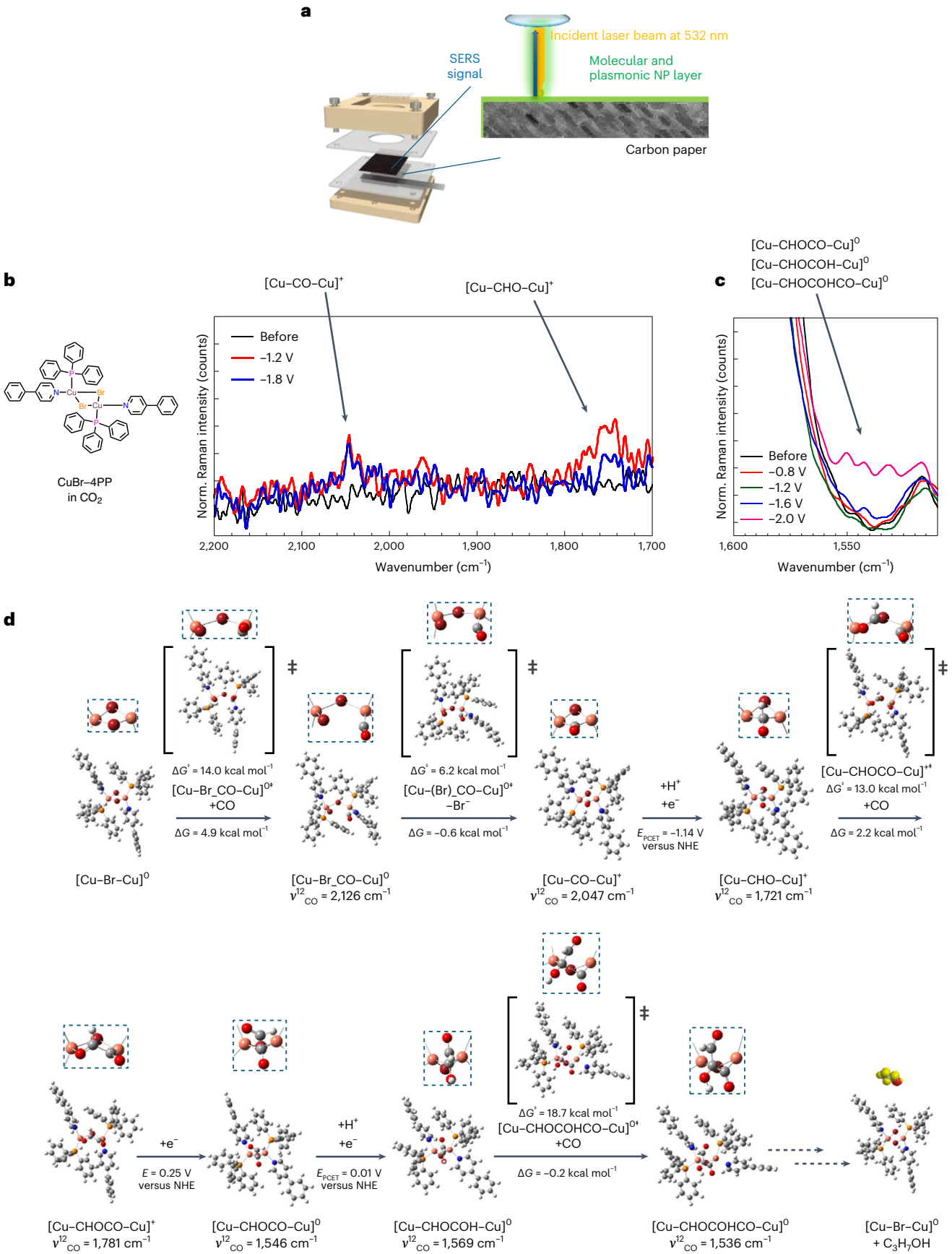

Fig. 3 | Mechanistic study elucidating the C_3 intermediate. a, Molecular operando SERS measurement system. **b**,**c**, Operando SERS spectra for CuBr–4PP under CO_2 for 1,700–2,200 cm^{-1} (**b**) and 1,510–1,600 cm^{-1} (**c**). **d**, Calculated CORR electrocatalytic reaction for CuBr–4PP via a protonation–electron coupling pathway using DFT calculations (Supplementary Data 1). Calculated reaction free-energy changes (ΔG) and reduction potentials (E) are reported in units of kcal mol^{-1} and volts versus NHE, respectively. The dashed frames above structures are enlarged views of the areas around the Cu centres.

to the promotion of C–C coupling and suppression of H_2 production. Operando spectroscopic analysis for the CO_2RR with $^{13}CO_2$ and using surface plasmons enabled the identification of intermediates important for C_3 formation. Investigations using DFT calculations found a mechanism that can explain both the operando measurements and energetics. The results suggest that the catalyst produces C_3 products by forming an intermediate species via C–C coupling between two Cu centres and flexibly varying the distance between them. To the best of our knowledge, previous examples of a molecular catalyst that generates C_3 products from CO_2 have remained elusive. The achievement of C–C coupling by the CO_2RR in a metal complex that can freely adjust the electronic state of the reaction centre and the reaction environment while maintaining its structure may be a major step towards the selective synthesis of higher value-added multicarbon products.

Methods

Materials

Copper(I) bromide (CuBr), potassium bicarbonate ($KHCO_3$) and all solvents were purchased from Fujifilm Wako Pure Chemical. PPh_3, 4PP, 12B and BisM were purchased from Tokyo Chemical Industry. All chemicals were used without further purification. Water-repellent treated CP (TGP-H-060-H) was purchased from Chemix.

Synthesis of CuBr–4PP

An acetone solution (10 ml) containing both 4PP (84 mg) and PPh_3 (130 mg) was added to a solution of CuBr (71 mg) in CH_3CN (MeCN). The mixture was stirred at room temperature overnight and then distilled under reduced pressure and washed with $(CH_3)_2CO$ and ethanol. It was further purified by silica gel in the order of 100% CH_2Cl_2, 99% CH_2Cl_2 and 1% MeCN, then dried in vacuum to synthesize the CuBr–4PP. The product was recrystallized from CH_2Cl_2 and Et_2O under light-shielded conditions. The yield was 71%.

Crystal data for $C_{29}H_{24}BrCuNP$

M = 560.91 g mol^{-1}, triclinic, space group P-1 (no. 2), a = 9.0996(2) Å, b = 10.62300(10) Å, c = 13.6314(2) Å, α = 94.7800(10)°, β = 108.785(2)°, γ = 95.6320(10)°, V = 1232.20(4) Å^3, Z = 2, T = 123.15 K, μ(Mo Kα) = 2.590 mm^{-1}, D_{calc} = 1.512 g cm^{-3}; 11,783 reflections were measured (3.882° ≤ 2Θ ≤ 62.392°), 6,761 of them unique (R_{int} = 0.0187, R_{sigma} = 0.0318), which were used in all calculations. The final R_1 was 0.0282 ($I > 2\sigma(I)$), and wR_2 was 0.0690 (all data).

Synthesis of CuBr–12B

A toluene solution (20 ml) containing 1,2-bis(diphenylphosphino) benzene (0.5 mmol, 223 mg) was added to CuBr (0.5 mmol). The mixture was stirred for 5 h at room temperature and then distilled under reduced pressure[32]. The product was washed with toluene, ethanol and methanol, then recrystallized from CH_2Cl_2 and Et_2O under light-shielded conditions. The yield was 55%.

Crystal data for $C_{60}H_{48}Br_2Cu_2P_4$

M = 1,179.76 g mol^{-1}, monoclinic, space group $P2_1$ (no. 4), a = 11.1978(4) Å, b = 18.7133(6) Å, c = 12.1395(4) Å, β = 97.551(3)°, V = 2,521.75(15) Å^3, Z = 2, T = 123.15 K, μ(Mo Kα) = 2.595 mm^{-1}, D_{calc} = 1.554 g cm^{-3}, 21,620 reflections measured (4.024° ≤ 2Θ ≤ 56.558°), 11,385 of them unique (R_{int} = 0.0579, R_{sigma} = 0.1064), which were used in all calculations. The final R_1 was 0.0635 ($I > 2\sigma(I)$), and wR_2 was 0.1107 (all data).

Synthesis of CuBr–BisM

A toluene solution (40 ml) containing bis(diphenylphosphino)methane (2 mmol, 840 mg) was added to CuBr (2 mmol). The mixture was stirred overnight at room temperature and then distilled under reduced pressure. The product was washed with toluene and acetone and subsequently recrystallized from CH_2Cl_2 and Et_2O under light-shielded conditions. The yield was 61%.

Crystal data for $C_{75}H_{66}Br_3Cu_3P_6$ + C_4H_9O

M_r = 1,584.56 + 73 g mol^{-1}, orthorhombic, space group $Pbca$ (no. 61), a = 15.7124(2) Å, b = 25.0060(3) Å, c = 36.9047(5) Å, $\alpha = \beta = \gamma$ = 90°, V = 14,500.0(3) Å^3, Z = 8, T = 123.15 K, μ(Mo Kα) = 2.708 mm^{-1}, D_{calc} = 1.519 g cm^{-3}, 106,977 reflections measured (3.254° ≤ 2Θ ≤ 58.26°), 19,341 of them unique (R_{int} = 0.0837, R_{sigma} = 0.0645), which were used in all calculations. The final R_1 was 0.0578 ($I > 2\sigma(I)$), and wR_2 was 0.1373 (all data).

Fabrication of CuBr complex molecular electrodes

A cathode was prepared by placing 1 mg of CuBr molecular powder directly on the centre (1 cm^2) of a piece of CP (~4 cm^2) and rubbing it with a spatula. It contained no additives such as binders or additional carbon products.

Characterization

CO_2 adsorption/desorption isotherms were recorded using an Autosorb-1 set-up (Quantachrome) at room temperature. Only powdered CuBr complexes and CuBr were measured.

The surface analysis of the electrode was performed using XPS (Ulvac Phi, Quantera SXM) with a monochromatic Al Kα X-ray source (1,486.6 eV), a photoelectron take-off angle of 45° and an analysis area with a diameter of 200 μm. Charge-up correction was performed using the C 1*s* 285-eV peak.

The chemical states of Cu and Br were evaluated by XAFS spectroscopy using the quick-XAFS technique[50]. Cu K-edge XANES spectra and extended XAFS (EXAFS) spectra were acquired in transmission mode at the BL33XU beamline of SPring-8. Boron nitride (100 mg) and the CuBr metal complexes were ground in an agate mortar and then moulded into pellets for transmission XAFS measurements. For CO_2 electrolysis in the operando XAFS measurement, a CuBr–4PP, CuBr–12B, CuBr–BisM or HKUST-1 (Sigma-Aldrich, Basolite C 300, 1 mg)/CP electrode was used as the working electrode (WE), an Ag/AgCl electrode (EC Frontier, RE-T14) as the reference electrode (RE) and a Pt-foil electrode (Niraco, PT-353212, diameter of 20 mm × 0.02 mm, 99.98%) as the counter electrode (CE). The WE had a Kapton film window for fluorescence XAFS measurements. During the operando XAFS measurements, CO_2 continuously flowed into the WE (cathode) side of the cell. The applied potential was controlled using a bipotentiostat (model 2325, ALS). The chemical states of Cu for CuBr–4PP in MeCN were studied from operando Cu K-edge XANES spectra in a three-pole electrolysis cell. Operando XAFS experiments were carried out by dissolving 0.5 mM CuBr–4PP in a MeCN electrolyte containing 0.1 M $NEt_4^+BF_4^-$ and aerated with CO_2 before performing constant-potential electrolysis measurements. A three-pole cell with CP as the WE, Pt as the CE and 0.01 M Ag/$AgNO_3$ as the RE was used. The constant-potential electrolysis of the CuBr–4PP molecule was performed using a potentiostat/galvanostat (Bio-Logic Science Instruments, SP-150).

Transmission electron microscopy observations were carried out using a JEM-2100F (JEOL) field-emission transmission electron microscope operating at an acceleration voltage of 200 kV.

Electrochemical measurements were conducted using a potentiostat/galvanostat (Bio-Logic Science Instruments, SP-150). The WE was combined with Ta foil as a contact material, and Pt foil and an Ag/AgCl electrode (RE-T14, EC Frontier) were used as the CE and RE, respectively. The H-type electrolysis cell used for electrocatalytic CO_2 reduction was composed of an anode and a cathode separated by an anion-exchange membrane (Astom). The electrolyte used was a CO_2-saturated 0.5 M aqueous solution of $KHCO_3$. All applied potentials were determined without *iR* compensation.The gas-phase CO_2 reduction product amounts were determined through in situ measurements using an H-type electrolysis flow cell in combination with gas chromatography (GC). The H-type electrolysis flow cell was equipped with an autosampler for in situ analyses and was directly connected to a GC system (SRI Instruments, Multiple Gas Analyzer #5) equipped

with Molecular Sieve SA and Hayesep-D columns. At the start of each experiment, CO_2 was passed through at a rate of 10 ml min^{-1} for 10 min to saturate the electrolyte and to remove air from the reactor. The quantities of gaseous products were estimated by multiplication of the concentration of the products determined using GC, the measurement interval (20 min) and the flow rate. Additionally, the quantity of $HCOO^-$ was measured using ion chromatography (Dionex, ICS-2100) with IonPacAS15 and IonPacAG15 columns, while maintaining the column temperature at 308 K. The alcohol content was determined using GC-MS (GCMS-QP2010, Shimadzu Corp.) with a CP-Volamine column. The error bars in plots correspond to the standard error (s.e.) of three independent measurements.

The gas-phase CO-reduction product amounts were determined through in situ measurements using an H-type electrolysis flow cell in combination with GC. The H-type electrolysis flow cell was equipped with an autosampler for in situ analyses and was directly connected to a GC system (SRI Instruments, Multiple Gas Analyzer #5) equipped with Molecular Sieve SA and Hayesep-D columns. At the start of each experiment, CO was passed through at a rate of 10 ml min^{-1} for 10 min to saturate the electrolyte and to remove air from the reactor. The quantities of gaseous products were estimated by the multiplication of the concentration of the products determined using GC, the measurement interval (10 min) and the flow rate. The amounts of alcohol, aldehyde and acetate were determined using GC-MS (GCMS-QP2010, Shimadzu Corp.) with a CP-Volamine column. The amount of CH_3COOH was measured using ion chromatography (Dionex, ICS-2100) with IonPacAS15 and IonPacAG15 columns, while maintaining the column temperature at 308 K.

Cyclic voltammetry measurements of each CuBr metal complex molecule were carried out by dissolving 0.5 mM CuBr metal complex molecule in a MeCN electrolyte containing 0.1 M NEt_4BF_4, followed by aeration with Ar or CO_2. A three-pole cell with a GC electrode as the WE, Pt as the CE, and a 0.01 M $Ag/AgNO_3$ electrode as the RE was used. Cyclic voltammetry of each CuBr complex molecule was performed using a potentiostat/galvanostat (Bio-Logic Science Instruments, SP-150) at a sweep rate of 25 mV s^{-1}. In situ UV spectra measurements were measured in MeCN containing 0.1 M $NEt_4^+BF_4^-$ as the supporting electrolyte and using a potentiostat/galvanostat (Bio-Logic Science Instruments, SP-150) and a conventional three-electrode-type cell. The cell consisted of an anode and a cathode separated by a cation-exchange membrane (Nafion 117) and was maintained at room temperature under an Ar or CO_2 atmosphere.

To verify the carbon source for the CO, CH_4 and C_2H_4 generated by electrolysis using CuBr–4PP, $^{13}CO_2$ isotope tracer analysis was performed. The three-electrode electrochemical cell was purged with 99% Isotec $^{13}CO_2$ gas by bubbling for 10 min and then sealed with a septum. To prevent carbon exchange between CO_2 and HCO_3^-, 0.5 M $KH^{13}CO_3$ was used as an electrolyte. After 10 min of electrolysis at −2.0 V versus Ag/AgCl (in 0.5 M $KH^{13}CO_3$), the gaseous reaction products were analysed using GC-MS (GC-MS-QP2010, Shimadzu) with an RT-Msieve 5 A column. In addition, the carbon source of the C_3H_7OH product was analysed using a three-electrode electrochemical cell purged with $^{13}CO_2$ gas (99%, Isotec). To avoid carbon exchange between the CO_2 and HCO_3^-, 0.5 M $KH^{13}CO_3$ was used as an electrolyte. After 20 min of electrolysis at −2.0 V versus Ag/AgCl, we analysed the mass number of PrOH using GC-MS (GC-MS; GCMS-QP2010, Shimadzu Corp.) with a CP-Volamine column.

Differential electrochemical MS was carried out using a mass spectrometer (JMS-Q1500, JEOL) coupled to a potentiostat/galvanostat (Bio-Logic Science Instruments, SP-150).

Operando Raman spectroscopy and SERS spectroscopy were performed using an excitation laser with a wavelength of 532 nm and an NRS-3300 (Jasco) or RAMANtouch (Nanophoton) Raman spectrometer. The intensity of the laser beam was 1 mW (normal measure) or ~0.1 mW (SERS), and the acquisition time for one Raman spectrum was 20–120 s. During this process, the sample electrode (Ta foil as a contact material), Pt foil and an Ag/AgCl electrode (RE-T14, EC Frontier) were used as the WE, CE and RE, respectively. The electrolysis cell for operando Raman spectroscopy and SERS consisted of an anode and a cathode separated by an anion-exchange membrane (Astom), together with a CO_2-saturated 0.5 M aqueous solution of $KHCO_3$ as the electrolyte. At the start of each experiment, CO_2 flowed at ~10 ml min^{-1} for 10 min to saturate the electrolyte and remove air in the reactor. During the operando measurement, CO_2 continuously flowed into the WE (cathode) side of the cell. The electrochemical reaction of the CuBr–4PP metal complex or HKUST-1 was measured using a bipotentiostat (model 2325, BAS). For the SERS electrode, a mixture of 10 µl of silica-shelled Ag nanoplates (NCXSPSH550-1ML, Sigma-Aldrich) and 1 mg of CuBr molecular was used. The localized surface plasmon resonance was adjusted to 550 nm to match the laser excitation wavelength, and the silica-shelled Ag nanoplates themselves did not exhibit CO_2 catalytic activity. During the isotope labelling experiment with $^{13}CO_2$, the reactors and CO_2RR conditions remained the same, whereas the operando SERS experiments were performed with a change from CO_2 to $^{13}CO_2$.

After the electrochemical measurements, the CuBr metal complex sample was removed from the CP using sonication and then cast or filtered for XAFS measurements and transmission electron microscopy observations. Dynamic light scattering measurements were used to analyse the electrolyte before and after the reaction using NanoPartica SZ-100-Z-100 (Horiba). XPS measurements were also performed for the CuBr–4PP on CP.

Calculations

All theoretical data were obtained from DFT calculations using the ωB97XD functional[51], performed within Gaussian 16[52]. The def2-SVP basis set[53] was used for H, C, N, P and Cu, and the def2-SVPD basis set[54,55] for Br and substrate-derived C and O, which are assumed to be anionic. Solvent effects in water were also estimated using the polarizable continuum model[56–58]. After optimization of molecular geometries, vibrational analyses were executed for the optimized geometries and the absence of an imaginary number frequency was confirmed for all optimized structures. The computed vibrational frequencies for the IR spectra were corrected by a scaling factor of 0.957, estimated from the CO molecule. To obtain the transition state of the thermal process, the reaction pathway was optimized using the nudged elastic band method[59] using the Reaction Plus Pro 2 software package (HPC Systems). The calculated candidate structures were then optimized using the synchronous transit-guided quasi-newton method to obtain a transition state with a single number of imaginary oscillations. The transition-state structures were characterized by intrinsic reaction coordinate calculations. The Gibbs free energies based on the rigid-rotor-harmonic-oscillator (RRHO) approximation (G^{RRHO}) were modified to the quasi-harmonic-treated G^{qh} by correcting the entropies[60] and enthalpies[61] using the GoodVibes toolkit[62] with a cut-off frequency of 100 cm^{-1}. The G^{qh} values were evaluated at 298.15 K and adjusted to the standard state concentration of 1 M (ref. 61). The Cartesian coordinates are shown in Supplementary Table 12 and Supplementary Data 1. Because the binuclear Cu complex can have various spin states[63,64], singlets and triplets were evaluated for species with even electrons, and doublets and quartets for species with odd electrons (Supplementary Fig. 12). All intermediates were more stable in the lower spin state, and the effect of spin contamination was confirmed to be small. For the reaction free-energy calculations, we used the explicit solvation energy of a proton in water (−265.9 kcal mol^{-1})[65]. The calculated free-energy changes were converted by the absolute standard potential for the hydrogen electrode (E_{NHE} = −4.281 V)[66]. The calculations for the first and second vertical electron affinities were performed with the def2-SVP basis set for Cu atoms, and the 6–31+G(d)[67–69] basis set for the other elements, because the extra electrons in anionic species have a spatially diffused character.

Data availability

The data supporting the findings of this study are available within the Article and its Supplementary Information or from the corresponding authors upon reasonable request. Crystallographic data for the structures reported in this Article have been deposited at the Cambridge Crystallographic Data Centre, under deposition nos. CCDC 2204883 (CuBr−4PP), 2235053 (CuBr−12B) and 2235326 (CuBr−BisM). Copies of the data can be obtained free of charge via https://www.ccdc.cam.ac.uk/structures/. The optimized structures from the DFT calculations are provided in Supplementary Data 1. Source data are provided with this paper.

References

1. Greenblatt, J. B., Miller, D. J., Ager, J. W., Houle, F. A. & Sharp, I. D. The technical and energetic challenges of separating (photo) electrochemical carbon dioxide reduction products. *Joule* **2**, 381–420 (2018).
2. Grim, R. G. et al. Transforming the carbon economy: challenges and opportunities in the convergence of low-cost electricity and reductive CO_2 utilization. *Energy Environ. Sci.* **13**, 472–494 (2020).
3. Bushuyev, O. S. et al. What should we make with CO_2 and how can we make it? *Joule* **2**, 825–832 (2018).
4. Sisler, J. et al. Ethylene electrosynthesis: a comparative techno-economic analysis of alkaline vs membrane electrode assembly vs CO_2-CO-C_2H_4 tandems. *ACS Energy Lett.* **6**, 997–1002 (2021).
5. Lum, Y. & Ager, J. W. Evidence for product-specific active sites on oxide-derived Cu catalysts for electrochemical CO_2 reduction. *Nat. Catal.* **2**, 86–93 (2019).
6. Tan, Y. C., Lee, K. B., Song, H. & Oh, J. Modulating local CO_2 concentration as a general strategy for enhancing C-C coupling in CO_2 electroreduction. *Joule* **4**, 1104–1120 (2020).
7. Wang, X. et al. Efficient electrosynthesis of *n*-propanol from carbon monoxide using a Ag–Ru–Cu catalyst. *Nat. Energy* **7**, 170–176 (2022).
8. Todorova, T. K., Schreiber, M. W. & Fontecave, M. Mechanistic understanding of CO_2 reduction reaction (CO_2RR) toward multicarbon products by heterogeneous copper-based catalysts. *ACS Catal.* **10**, 1754–1768 (2019).
9. Chen, J. & Wang, L. Effects of the catalyst dynamic changes and influence of the reaction environment on the performance of electrochemical CO_2 reduction. *Adv. Mater.* **34**, 2103900 (2022).
10. Liang, H. Q., Beweries, T., Francke, R. & Beller, M. Molecular catalysts for reductive homocoupling of CO_2 towards C_{2+} compounds. *Angew. Chem. Int. Ed.* **61**, e202200723 (2022).
11. Sun, L., Reddu, V., Fisher, A. C. & Wang, X. Electrocatalytic reduction of carbon dioxide: opportunities with heterogeneous molecular catalysts. *Energy Environ. Sci.* **13**, 374–403 (2020).
12. Dalle, K. E. et al. Electro- and solar-driven fuel synthesis with first row transition metal complexes. *Chem. Rev.* **119**, 2752–2875 (2019).
13. Boutin, E. & Robert, M. Molecular electrochemical reduction of CO_2 beyond two electrons. *Trends Chem.* **3**, 359–372 (2021).
14. Tang, T. et al. Optimizing the electrocatalytic selectivity of carbon dioxide reduction reaction by regulating the electronic structure of single-atom M-N-C materials. *Adv. Funct. Mater.* **32**, 2111504 (2022).
15. Sakamoto, N. et al. Electrochemical CO_2 reduction improved by tuning the Cu-Cu distance in halogen-bridged dinuclear cuprous coordination polymers. *J. Catal.* **404**, 12–17 (2021).
16. Sakamoto, N. et al. Self-assembled cuprous coordination polymer as a catalyst for CO_2 electrochemical reduction into C_2 products. *ACS Catal.* **10**, 10412–10419 (2020).
17. Wang, R. et al. Proton/electron donors enhancing electrocatalytic activity of supported conjugated microporous polymers for CO_2 reduction. *Angew. Chem. Int. Ed.* **61**, e202115503 (2022).
18. Polyansky, D. E., Grills, D. C., Ertem, M. Z., Ngo, K. T. & Fujita, E. Role of bimetallic interactions in the enhancement of catalytic CO_2 reduction by a macrocyclic cobalt catalyst. *ACS Catal.* **12**, 1706–1717 (2022).
19. Rivera Cruz, K. E., Liu, Y., Soucy, T. L., Zimmerman, P. M. & McCrory, C. C. Increasing the CO_2 reduction activity of cobalt phthalocyanine by modulating the σ-donor strength of axially coordinating ligands. *ACS Catal.* **11**, 13203–13216 (2021).
20. Rønne, M. H. et al. Ligand-controlled product selectivity in electrochemical carbon dioxide reduction using manganese bipyridine catalysts. *J. Am. Chem. Soc.* **142**, 4265–4275 (2020).
21. Balamurugan, M. et al. Electrocatalytic reduction of CO_2 to ethylene by molecular Cu-complex immobilized on graphitized mesoporous carbon. *Small* **16**, 2000955 (2020).
22. Lu, Y.-F. et al. Predesign of catalytically active sites via stable coordination cluster model system for electroreduction of CO_2 to ethylene. *Angew. Chem. Int. Ed.* **60**, 26210 (2021).
23. Weng, Z. et al. Active sites of copper-complex catalytic materials for electrochemical carbon dioxide reduction. *Nat. Commun.* **9**, 415 (2018).
24. Zhu, Q. et al. Carbon dioxide electroreduction to C_2 products over copper-cuprous oxide derived from electrosynthesized copper complex. *Nat. Commun.* **10**, 3851 (2019).
25. Ren, S. et al. Electrocatalysts derived from copper complexes transform CO into C_{2+} products effectively in a flow cell. *Chem. Eur. J.* **28**, e202200340 (2022).
26. Zheng, Y. et al. Understanding the roadmap for electrochemical reduction of CO_2 to multi-carbon oxygenates and hydrocarbons on copper-based catalysts. *J. Am. Chem. Soc.* **141**, 7646–7659 (2019).
27. Espinal, L. et al. Time-dependent CO_2 sorption hysteresis in a one-dimensional microporous octahedral molecular sieve. *J. Am. Chem. Soc.* **134**, 7944–7951 (2012).
28. Yamazaki, Y., Miyaji, M. & Ishitani, O. Utilization of low-concentration CO_2 with molecular catalysts assisted by CO_2-capturing ability of catalysts, additives or reaction media. *J. Am. Chem. Soc.* **144**, 6640–6660 (2022).
29. Nakaya, M. et al. CO_2-induced spin-state switching at room temperature in a monomeric cobalt(II) complex with the porous nature. *Angew. Chem. Int. Ed.* **59**, 10658 (2020).
30. Chen, L., Cao, F. & Sun, H. Ab initio study of the π-π interactions between CO_2 and benzene, pyridine and pyrrole. *Int. J. Quantum Chem.* **113**, 2261–2266 (2013).
31. Lee, H. M., Youn, I. S., Saleh, M., Lee, J. W. & Kim, K. S. Interactions of CO_2 with various functional molecules. *Phys. Chem. Chem. Phys.* **17**, 10925–10933 (2015).
32. Yang, R.-N. et al. Synthesis, structure and characterization of the trinuclear copper(I) complex $[Cu_3(\mu_3\text{-}Br)_2(dppm)_3]Br$. *Chin. J. Chem.* **17**, 284–292 (1999). .
33. Lang, J.-P. & Tatsumi, K. Low temperature solid-state reactions of $(NH_4)_2[MS_4]$ (M=W, Mo) with $[Cu(CH_3CN)_4](PF_6)$ and CuBr in the presence of bis(diphenylphosphino)methane (dppm): crystal structures of $[MS_4Cu_4(dppm)_4](PF_6)_2$ (M=W, Mo), $[WS_4Cu_3(dppm)_3]X$ (X=PF_6, Br), $[Cu_3(dppm)_3Br_2]Br$, $[WS_4Cu_2(dppm)_3]$, and $[(n\text{-}Bu)_4N][WS_4Cu_3Br_2(dppm)_2]$. *Inorg. Chem.* **37**, 6308–6316 (1998).
34. Liang, W. et al. Copper-catalyzed [3+2] cycloaddition reactions of isocyanoacetates with phosphaalkynes to prepare 1,3-azaphospholes. *Angew. Chem. Int. Ed.* **58**, 1168–1173 (2019).
35. Tsuboyama, A. et al. Photophysical properties of highly luminescent copper(I) halide complexes chelated with 1,2-bis (diphenylphosphino) benzene. *Inorg. Chem.* **46**, 1992–2001 (2007).

36. Aslanidis, P., Cox, P. J., Kaltzoglou, A. & Tsipis, A. C. An experimental and theoretical (DFT) investigation of the coordination mode of 2,4-dithiouracil (2,4-dtucH_2) in copper(I) complexes with 1,2-bis(diphenylphosphanyl)benzene (dppbz): the crystal structures of [Cu(μ-Br)(dppbz)]$_2$ and [CuBr(dppbz)(2,4-dtucH_2)]. *Eur. J. Inorg. Chem.* **2**, 334–344 (2006).
37. Tsuge, K. et al. Luminescent copper(I) complexes with halogenido-bridged dimeric core. *Coord. Chem. Rev.* **306**, 636–651 (2016).
38. Lamagni, P. et al. Graphene inclusion controlling conductivity and gas sorption of metal-organic framework. *RSC Adv.* **8**, 13921–13932 (2018).
39. Sharma, V., Schlücker, S. & Srivastava, S. K. Origin of the blue-shifted hydrogen bond in the vibrational Raman spectra of pyridine-water complexes: a density functional theory study. *J. Raman Spectrosc.* **52**, 1722–1734 (2021).
40. Zhan, C. et al. Revealing the co coverage-driven C-C coupling mechanism for electrochemical CO_2 reduction on Cu_2O nanocubes via operando Raman spectroscopy. *ACS Catal.* **11**, 7694–7701 (2021).
41. Tzschoppe, M., Huck, C., Vogt, J., Neubrech, F. & Pucci, A. Impact of metal-optical properties on surface-enhanced infrared absorption. *J. Phys. Chem. C* **122**, 15678–15687 (2018).
42. Katayama, Y. et al. An in situ surface-enhanced infrared absorption spectroscopy study of electrochemical CO_2 reduction: selectivity dependence on surface C-bound and O-bound reaction intermediates. *J. Phys. Chem. C* **123**, 5951–5963 (2018).
43. Zhao, Q., Martirez, J. M. P. & Carter, E. A. Charting C-C coupling pathways in electrochemical CO_2 reduction on Cu(111) using embedded correlated wavefunction theory. *Proc. Natl Acad. Sci. USA* **119**, e2202931119 (2022).
44. Santatiwongchai, J., Faungnawakij, K. & Hirunsit, P. Comprehensive mechanism of CO_2 electroreduction toward ethylene and ethanol: the solvent effect from explicit water-Cu(100) interface models. *ACS Catal.* **11**, 9688–9701 (2021).
45. Cheng, T., Xiao, H. & Goddard, W. A. Full atomistic reaction mechanism with kinetics for CO reduction on Cu(100) from ab initio molecular dynamics free-energy calculations at 298 K. *Proc. Natl Acad. Sci. USA* **114**, 1795–1800 (2017).
46. Dattila, F. et al. Modeling operando electrochemical CO_2 reduction. *Chem. Rev.* **122**, 11085–11130 (2022).
47. Pablo-García, S. et al. Mechanistic routes toward C_3 products in copper-catalysed CO_2 electroreduction. *Catal. Sci. Technol.* **12**, 409–417 (2022).
48. Kim, Y. et al. Time-resolved observation of C-C coupling intermediates on Cu electrodes for selective electrochemical CO_2 reduction. *Energy Environ. Sci.* **13**, 4301–4311 (2020).
49. Zhao, Y. et al. Elucidating electrochemical CO_2 reduction reaction processes on Cu(*hkl*) single-crystal surfaces by in situ Raman spectroscopy. *Energy Environ. Sci.* **15**, 3968–3977 (2022).
50. Nonaka, T. et al. Quick-scanning X-ray absorption spectroscopy system with a servo-motor-driven channel-cut monochromator with a temporal resolution of 10 ms. *Rev. Sci. Instrum.* **83**, 083112 (2012).
51. Chai, J.-D. & Head-Gordon, M. Long-range corrected hybrid density functionals with damped atom-atom dispersion corrections. *Phys. Chem. Chem. Phys.* **10**, 6615–6620 (2008).
52. Frisch, M. J. et al. *Gaussian 16* revision C.01 (Gaussian, 2016).
53. Weigend, F. & Ahlrichs, R. Balanced basis sets of split valence, triple zeta valence and quadruple zeta valence quality for H to Rn: design and assessment of accuracy. *Phys. Chem. Chem. Phys.* **7**, 3297–3305 (2005).
54. Rappoport, D. & Furche, F. Property-optimized Gaussian basis sets for molecular response calculations. *J. Chem. Phys.* **133**, 134105 (2010).
55. Cancès, E., Mennucci, B. & Tomasi, J. A new integral equation formalism for the polarizable continuum model: theoretical background and applications to isotropic and anisotropic dielectrics. *J. Chem. Phys.* **107**, 3032–3041 (1997).
56. Tomasi, J., Mennucci, B. & Cammi, R. Quantum mechanical continuum solvation models. *Chem. Rev.* **105**, 2999–3093 (2005).
57. Scalmani, G. & Frisch, M. J. Continuous surface charge polarizable continuum models of solvation. I. General formalism. *J. Chem. Phys.* **132**, 114110 (2010).
58. Henkelman, G. & Jónsson, H. Improved tangent estimate in the nudged elastic band method for finding minimum energy paths and saddle points. *J. Chem. Phys.* **113**, 9978–9985 (2000).
59. Grimme, S. Supramolecular binding thermodynamics by dispersion-corrected Density Functional Theory. *Chem. Eur. J.* **18**, 9955–9964 (2012).
60. Li, Y.-P., Gomes, J., Mallikarjun Sharada, S., Bell, A. T. & Head-Gordon, M. Improved force-field parameters for QM/MM simulations of the energies of adsorption for molecules in zeolites and a free rotor correction to the rigid rotor harmonic oscillator model for adsorption enthalpies. *J. Phys. Chem. C* **119**, 1840–1850 (2015).
61. Luchini, G., Alegre-Requena, J., Funes-Ardoiz, I. & Paton, R. GoodVibes: automated thermochemistry for heterogeneous computational chemistry data. *F1000Res.* **9**, 291 (2020).
62. Ziegler, M. S., Levine, D. S., Lakshmi, K. V. & Tilley, T. D. Aryl group transfer from tetraarylborato anions to an electrophilic dicopper(I) center and mixed-valence μ-aryl dicopper(I,II) complexes. *J. Am. Chem. Soc.* **138**, 6484–6491 (2016).
63. Desnoyer, A. N. et al. A dicopper nitrenoid by oxidation of a Cu^ICu^I core: synthesis, electronic structure and reactivity. *J. Am. Chem. Soc.* **143**, 7135–7143 (2021).
64. Kelly, C. P., Cramer, C. J. & Truhlar, D. G. Aqueous solvation free energies of ions and ion-water clusters based on an accurate value for the absolute aqueous solvation free energy of the proton. *J. Phys. Chem. B* **110**, 16066–16081 (2006).
65. Isse, A. A. & Gennaro, A. Absolute potential of the standard hydrogen electrode and the problem of interconversion of potentials in different solvents. *J. Phys. Chem. B* **114**, 7894–7899 (2010).
66. Krishnan, R., Binkley, J. S., Seeger, R. & Pople, J. A. Self-consistent molecular orbital methods. XX. A basis set for correlated wave functions. *J. Chem. Phys.* **72**, 650–654 (1980).
67. McLean, A. D. & Chandler, G. S. Contracted Gaussian basis sets for molecular calculations. I. Second row atoms, *Z*=11–18. *J. Chem. Phys.* **72**, 5639–5648 (1980).
68. Francl, M. M. et al. Self-consistent molecular orbital methods. XXIII. A polarization-type basis set for second-row elements. *J. Chem. Phys.* **77**, 3654–3665 (1982).
69. Clark, T., Chandrasekhar, J., Spitznagel, G. W. & Schleyer, P. V. R. Efficient diffuse function-augmented basis sets for anion calculations. III. The 3-21+G basis set for first-row elements, Li-F. *J. Comput. Chem.* **4**, 294–301 (1983).

Acknowledgements

The XAFS data were acquired at the BL33XU beamline of the SPring-8 facility with the approval of the Japan Synchrotron Radiation Research Institute (JASRI; proposal nos. 2019B7038, 2020A7038, 2021A7038, 2021B7038, 2022A7038 and 2022B7038). We thank Y. F. Nishimura, Y. Kato, T. M. Suzuki, M. Ohashi, N. Takahashi and S. Kosaka for useful discussions. We thank Y. Goto for assistance with the CO_2 absorption

experiments. M. Murase is thanked for providing advice regarding the single-crystal X-ray structure analysis.

Author contributions

N.S., K.S. and T.M. supervised the project. N.S. and K.S. conceived the concept of the catalyst. N.S. performed experiments and carried out data analysis. K.S. and S. Shirai performed calculations. T.N. and N.S. performed XAFS experiments and analyses. N.S., K.S. and S. Sato performed CO_2 reduction reaction experiments and absorption–desorption characteristic experiments. T.A. designed the electrochemical cells and performed operando MS experiments. All authors discussed the results, and the paper was written by N.S., K.S., S. Shirai and S. Sato, with assistance from all co-authors.

Competing interests

The authors declare no competing interests.

Additional information

Supplementary information The online version contains supplementary material available at https://doi.org/10.1038/s41929-024-01147-y.

Correspondence and requests for materials should be addressed to Naonari Sakamoto or Keita Sekizawa.

Peer review information *Nature Catalysis* thanks Julien Bonin, Peter Müller, Casey O'Brien and the other, anonymous, reviewer(s) for their contribution to the peer review of this work.